







# GDSR: Global-Detail Integration through Dual-Branch Network with Wavelet Losses for Remote Sensing Image Super-Resolution

Qiwei Zhu , Kai Li , Guojing Zhang , Xiaoying Wang , Jianqiang Huang , and Xilai Li 

**Abstract**—In recent years, deep neural networks, including Convolutional Neural Networks, Transformers, and State Space Models, have achieved significant progress in Remote Sensing Image (RSI) Super-Resolution (SR). However, existing SR methods typically overlook the complementary relationship between global and local dependencies. These methods either focus on capturing local information or prioritize global information, which results in models that are unable to effectively capture both global and local features simultaneously. Moreover, their computational cost becomes prohibitive when applied to large-scale RSIs. To address these challenges, we introduce the novel application of Receptance Weighted Key Value (RWKV) to RSI-SR, which captures long-range dependencies with linear complexity. To simultaneously model global and local features, we propose the Global-Detail dual-branch structure, GDSR, which performs SR reconstruction by paralleling RWKV and convolutional operations to handle large-scale RSIs. Furthermore, we introduce the Global-Detail Reconstruction Module (GDRM) as an intermediary between the two branches to bridge their complementary roles. In addition, we propose Wavelet Loss, a loss function that effectively captures high-frequency detail information in images, thereby enhancing the visual quality of SR, particularly in terms of detail reconstruction. Extensive experiments on several benchmarks, including AID, AID\_CDM, RSSRD-QH, and RSSRD-QH\_CDM, demonstrate that GDSR outperforms the state-of-the-art Transformer-based method HAT by an average of 0.05 dB in PSNR, while using only 63% of its parameters and 51% of its FLOPs, achieving an inference speed 2.9 times faster. Furthermore, the Wavelet Loss shows excellent generalization across various architectures, providing a novel perspective for RSI-SR enhancement.

**Index Terms**—remote sensing image, super-resolution, global-detail reconstruction, dual-branch.

## I. INTRODUCTION

This work was supported in part by the Natural Science Foundation of Qinghai Province (No. 2023-ZJ-906M) and the National Natural Science Foundation of China (No.U23A20159, No. 62162053, No.42265010). (*Corresponding author: Guojing Zhang; Xiaoying Wang.*)

Qiwei Zhu, Guojing Zhang, and Jianqiang Huang are with the School of Computer Technology and Application, Qinghai University, Xining 810016, China (e-mail: qiweizhu@qhu.edu.cn; zhanggj@qhu.edu.cn; 2011990026@qhu.edu.cn), and also with the Qinghai Provincial Laboratory for Intelligent Computing and Application, Qinghai University, Xining 810016, China.

Kai Li is with the Department of Computer Science and Technology, Tsinghua University, Beijing 100084, China (e-mail: lik24@mails.tsinghua.edu.cn).

Xiaoying Wang is with the School of Computer and Information Science, Qinghai Institute of Technology, Xining 810018, China (e-mail: wangxy@qh.it.edu.cn).

Xilai Li is with the College of Agriculture and Animal Husbandry, Qinghai University, Xining 810016, China (e-mail: 1985990024@qhu.edu.cn).

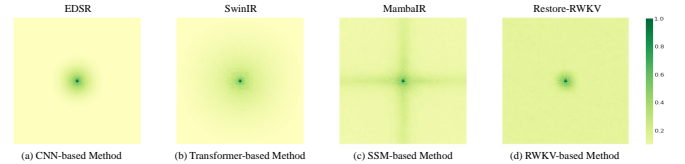


Fig. 1. The ERF [12] visualization for different models with different architectures. A more extensively distributed dark area indicates a larger ERF. The RWKV-based method Restore-RWKV [13] was restructured to be consistent with other models. It can be observed that the ERF of the model demonstrates a progressive enhancement when evaluated using CNN, Transformer, SSM, and RWKV.

THE rapid development of remote sensing technologies has resulted in an ever-increasing availability of satellite and aerial images, which play a crucial role in a variety of applications, such as environmental monitoring [1], urban planning [2], and disaster management [3]. However, the resolution of these remote sensing images is often constrained by the limitations of imaging sensors, atmospheric interference, and satellite bandwidth. Consequently, SR techniques, which seek to reconstruct high-resolution (HR) images from low-resolution (LR) observations, have garnered significant interest from both academic and industrial sectors [4], [5]. In particular, remote sensing image super-resolution (RSISR) has emerged as a pivotal research area that enhances spatial resolution and reveals finer details that are essential for accurate analysis.

Traditional SR methods have been dominated by Convolutional Neural Networks (CNNs) [6], [7] due to their strong local feature extraction and efficient computation. Models such as SRResNet [8] and EDSR [9] have demonstrated that deeper CNNs can progressively enhance SR performance. However, they suffer from the Effective Receptive Field (ERF) problem (as depicted in Fig. 1 (a)). Although deeper networks theoretically have larger receptive fields, only a small portion is effectively utilized during feature extraction, which limits their ability to capture long-range dependencies. This becomes particularly challenging in RSIs, where diverse spatial patterns and textures overwhelm the limited modeling capacity of CNN-based methods [10], [11].

In recent years, Transformers have gained significant traction in computer vision [14], [15], including RSISR [10], [16]. They excel at capturing global dependencies by modeling long-range interactions through self-attention mechanisms. However, the quadratic complexity of the self-attention operation can become a bottleneck when processing large-scale

satellites or aerial images. To address this, many Transformer-based models aim to reduce computational demands by limiting attention to smaller windows [14], which in turn reduces the effective receptive field (as shown in Fig. 1 (b)) and conflicts with the goal of capturing long-range dependencies. Additionally, HAT [15] combines channel attention and window-based self-attention with an overlapping cross-attention module to capture long-range dependencies. However, although transformers can capture the global context, they struggle with computational complexity and may lose structural information during sequence transformation [17], necessitating a re-evaluation of existing methods and the development of novel approaches.

The linear architecture of Transformers like Mamba-based models [18] and RWKV-based models [13] serves as an efficient alternative to Transformers. Mamba-based models leverage State Space Models (SSMs) [19] to causally capture long-range dependencies with linear computational complexity, with recent studies suggesting that they can achieve performance comparable to or even better than Transformer-based models [18], [20]. However, their inherent sequence modeling in SSMs still poses challenges in achieving an optimal ERF for 2D images (as depicted in Fig. 1 (c)). RWKV-based models [21], [22], originally developed for natural language processing (NLP), has emerged as a potential alternative to the transformer and amba. RWKV improves efficiency with linear complexity for long-range dependencies and better captures local dependencies, enhancing performance on large-scale NLP and vision tasks. Recent studies have shown that RWKV-based models outperform Transformer-based models and linearly scaled Mamba-based models in terms of effectiveness and efficiency [22], [23]. Despite pioneering efforts to adopt RWKV for vision tasks, the adaptation of RWKV to the field of RSISR remains unexplored.

While CNNs, Transformers, Mamba, and RWKV networks each offer distinct advantages, the challenges of effectively managing receptive fields and addressing the ERF limitations remain open research questions in RSISR. Notably, a recent study [24] has shown that multi-head self-attention (MSA) and convolutional layers exhibit complementary filtering behaviors. Specifically, MSAs act as low-pass filters, emphasizing broader structures and smoothing noise, whereas conv layers serve as high-pass filters, focusing on fine-grained textures and edges. These contrasting properties make the combination of MSAs and conv layers particularly beneficial for improving model performance. Moreover, high-frequency details are crucial for accurately reconstructing remote sensing images, as they play a key role in preserving fine-grained information. However, existing approaches struggle to simultaneously model long-range dependencies while effectively capturing high-frequency details. Therefore, a natural question arises: *Can a more efficient yet effective solution be developed to capture long-range dependencies across large-scale RSIs with convolution, which directly handles 2D spatial structures and offers computational advantages, while also efficiently reconstructing high-frequency details?*

In this paper, we propose a novel approach that integrates global representations and detailed extraction with wavelet

losses to enhance the SR performance for remote sensing imagery. Our main contributions can be summarized as follows:

- 1) The RWKV is introduced for remote sensing image super-resolution, along with GDSR, a novel architecture designed to effectively combine global and local information through a dual-branch structure.
- 2) A Global–Detail Reconstruction Module (GDRM) is proposed to efficiently integrate information from the dual branches. By merging complementary features, this module enhances the synergy between the branches, thereby significantly improving the overall performance of RSISR tasks.
- 3) Wavelet loss is introduced as a simple yet powerful loss function for RSISR. This approach effectively enhanced both the PSNR and visual quality, and demonstrated robust performance improvements across various network architectures. Moreover, its ease of implementation and adaptability make it a practical and highly effective solution for advancing RSISR techniques.

We demonstrate the empirical validity of GDSR by comparing it with various competitive CNN-, GAN-, Transformer-, Mamba-, and hybrid-based models on two RSI benchmark datasets using two degradation methods showing SOTA results. In addition, we conducted extensive ablation experiments (as detailed in Section IV-C) to investigate the approach of global-detail integration and its effect on RSI-SR, and to examine the effect of Wavelet Loss on various model architectures. We believe our work will advance efficient large-scale RSI-SR, improving both fidelity and processing speed, while ensuring robustness and practical applicability for real-world remote sensing tasks.

## II. RELATED WORK

### A. Remote Sensing Image Super-resolution

Recent advances in deep learning have greatly improved RSI-SR, with methods typically falling into CNN-based, Transformer-based, and Mamba-based categories. CNN-based methods, inspired by SRCNN [6], have used modules like residual connections [7], dense structures [25], and attention mechanisms [26], [27] to enhance performance. However, they are limited by their inability to capture long-range dependencies, which hinders their effectiveness in large-scale RSI data. Transformer-based methods, leveraging self-attention (SA) [28], have shown promise in modeling global dependencies, with approaches like window-based SA [15] and recursive SA [29] attempting to address the quadratic complexity. However, SA remains inefficient for high-resolution images, often sacrificing global modeling capability. To overcome these limitations, Mamba-based methods, which offer linear complexity for global modeling, present a compelling solution. MambaIR [18] successfully introduced Mamba into the SR domain, while FreMamba [20] pioneers the exploration of Mamba’s potential for RSI-SR, extending it with frequency analysis. Due to the unidirectional nature of SSM, Mamba’s global dependency modeling still faces challenges in achieving accurate results for RSI-SR.

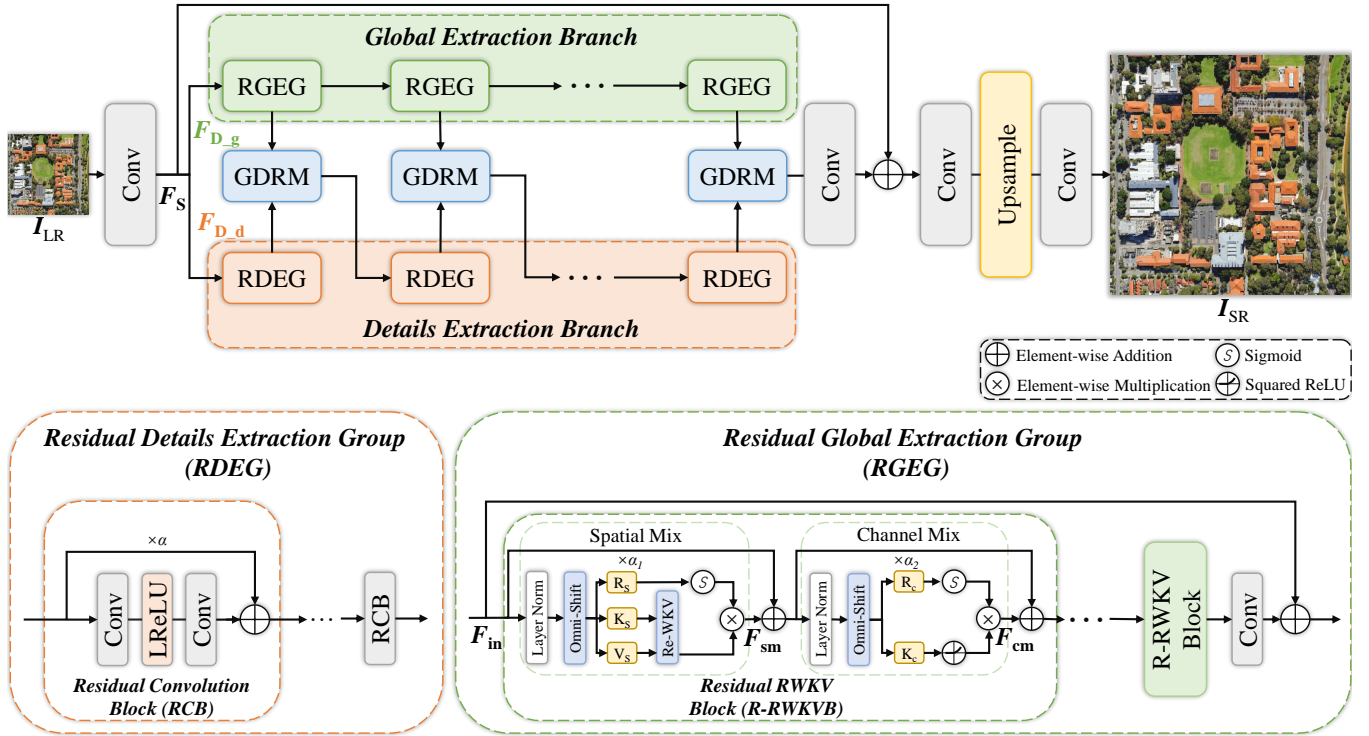


Fig. 2. Overview of the proposed GDSR.

### B. RWKV in computer vision

Recent studies [22] indicate that RWKV can outperform both Transformers and Mamba in NLP tasks. Vision-RWKV [30] has been successfully applied to vision tasks, showing superior performance compared to vision Transformers with lower computational complexity. Several RWKV-based models, such as Diffusion-RWKV [31] for image generation and Restore-RWKV [13] for medical image restoration, have demonstrated promising results. However, the potential of RWKV for RSI-SR remains unexplored. Given that RSI exhibits diverse and complex characteristics, with texture information often subtler than in natural images, it presents unique challenges for SR tasks. Moreover, critical high-frequency details tend to be lost in deep learning models, emphasizing the need for a more effective approach to capture these crucial components. This paper pioneers the exploration of RWKV’s potential for RSI-SR by introducing a novel dual-branch architecture that combines RWKV with convolutional operations.

### C. Wavelet Transforms in Deep Learning

The wavelet transform (WT) [32] has been a fundamental tool for signal processing since the 1980s and has more recently been integrated into neural network architectures for various tasks. Several studies have explored wavelet-domain methods for image restoration and SR tasks, recognizing the need to treat low- and high-frequency features differently. Methods like Wavelet-SRNet [33], WDST [34] and WDRN [35] predict wavelet coefficients to enhance SR performance. More recently, WGSr [36] introduced wavelet subband losses

in GAN-based SR models to better control artifacts. In addition, WTConv [37], a novel layer leveraging the wavelet transform to effectively expand the receptive field of convolutions, has been proposed as a drop-in replacement for depth-wise convolutions in CNNs, improving performance across several key computer vision tasks. In this paper, we propose a novel Wavelet Loss that directly optimizes the reconstruction of wavelet-domain features. Our approach is designed to complement SR models based on various architectures, including CNN, GAN, Transformer, and Mamba, as well as their hybrid combinations, which have demonstrated superior performance in RSISR. Unlike previous methods, our Wavelet Loss seamlessly integrated wavelet-based supervision into the end-to-end SR training framework to ensure effective high-frequency detail recovery.

## III. METHODOLOGY

In this section, we first introduce the overall structure of the proposed GDSR and then described three important modules in GDSR, namely RGEg, RDEg, and GDRM. Finally, we detail our designed loss function.

### A. Overview of GDSR

As illustrated in Fig. 2, GDSR begins by extracting the shallow feature  $F_S \in \mathbb{R}^{H \times W \times C}$  from the LR input using a convolutional layer. It then derives the deep features  $F_{D_g} \in \mathbb{R}^{H \times W \times C}$  and  $F_{D_d} \in \mathbb{R}^{H \times W \times C}$  through parallel branches: global extraction branch and details extraction branch, respectively. These features are subsequently fused using the GDRM. A global residual connection is then applied to combine the low-level and deep features, and finally, the

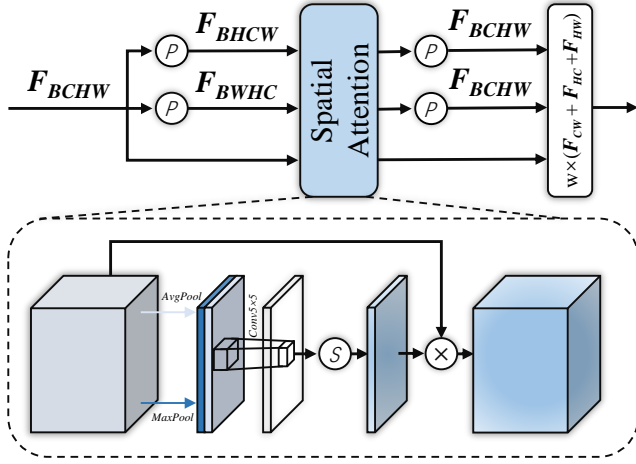


Fig. 3. Structure of PSAM.

pixel-shuffle method is employed for upsampling to generate the SR output.

The SR process of GDSR can be mathematically described as:

$$\mathbf{I}_{\text{SR}} = \text{Up}(\text{GDRM}(\mathbf{F}_{\text{D}_g}, \mathbf{F}_{\text{D}_d}) + \mathbf{F}_s), \quad (1)$$

where  $\text{Up}(\cdot)$  denotes the upsampling function and  $\text{GDRM}(\cdot)$  denotes the global-detail reconstruction operation.  $\mathbf{I}_{\text{SR}} \in \mathbb{R}^{(rH) \times (rW) \times 3}$  is the reconstructed SR image with a scaling factor of  $r$ .

### B. Residual Details Extraction Group

Deep convolutional networks have achieved remarkable advancements in SR tasks, with residual structures proving effective in addressing network degradation issues [9]. To harness these advantages, we propose RDEGs, which are structured as sequences of residual units, each referred to as a Residual Convolution Block (RCB). RCBs are specifically designed to enhance the recovery of fine details from LR inputs while maintaining stable and efficient model training.

A single RCB can be represented as:

$$\mathbf{F}_{l+1} = \alpha \mathbf{F}_l + W_1(\text{LReLU}(W_0 \mathbf{F}_l)), \quad (2)$$

where  $\mathbf{F}_l$  and  $\mathbf{F}_{l+1}$  represent the input and output feature maps of the  $l$ -th RCB, respectively.  $\alpha$  denotes a learnable scale factor that controls the amount of information passed through the residual connection.  $W_0$  and  $W_1$  denote the convolution operations in the RCB and LReLU refers to the Leaky ReLU activation function.

We concatenate  $N$  RCBs to form an RDEG module. The RDEG can be mathematically expressed as:

$$\text{RDEG}^k = \alpha \mathbf{F}_{\text{D}_d}^{N-1} + W_1(\text{LReLU}(W_0(\mathbf{F}_{\text{D}_d}^{N-1}))), N \geq 1, \quad (3)$$

where  $\mathbf{F}_{\text{D}_d}^0 = \text{RDEG}^{k-1}$ . Here,  $\text{RDEG}^k$  represents the feature map of the  $k$ -th RDEG,  $\mathbf{F}_{\text{D}_d}^{N-1}$  denotes the output of the  $(N-1)$ -th RCB within the  $k$ -th RDEG.

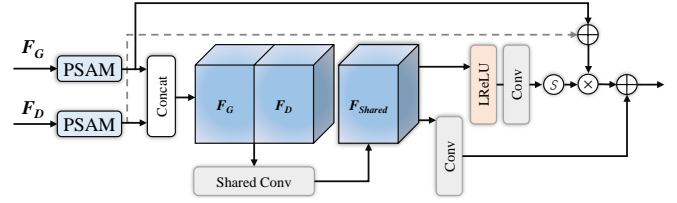


Fig. 4. Structure of GDRM.

### C. Residual Global Extraction Group

Inspired by the recent success of RWKV in computer vision applications [30], [13], we seek to utilize its strengths in modeling long-range dependencies in RSIs. As illustrated in Fig. 2, the proposed RGEG consists of multiple Residual RWKV Blocks (R-RWKVs). The spatial mix (sm) module is designed to establish long-range dependencies among tokens across the spatial dimension. Given an input feature flattened into a one-dimensional sequence  $\mathbf{F}_{\text{in}} \in \mathbb{R}^{T \times C}$ , where  $T = H \times W$  represents the total number of tokens, the spatial mix module begins by applying layer normalization (LN) followed by the Omni-Shift operation [13]. The output is then passed through three parallel linear projection layers to obtain the receptance  $R_s \in \mathbb{R}^{T \times C}$ , key  $K_s \in \mathbb{R}^{T \times C}$ , and value  $V_s \in \mathbb{R}^{T \times C}$ :

$$\mathbf{F}_s = \text{Omni-Shift}(\text{LN}(\mathbf{F}_{\text{in}})), \quad (4)$$

$$R_s = \mathbf{F}_s W_{R_s}, \quad K_s = \mathbf{F}_s W_{K_s}, \quad V_s = \mathbf{F}_s W_{V_s}, \quad (5)$$

where  $W_{R_s}$ ,  $W_{K_s}$ , and  $W_{V_s}$  are linear projection matrices. The key  $K_s$  and value  $V_s$  are then processed through the Re-WKV attention mechanism [13] to compute the global attention output  $O_{\text{attn}} \in \mathbb{R}^{T \times C}$ . Finally, the receptance  $R_s$ , after gating through a sigmoid function  $\sigma(\cdot)$ , modulates the attention output via element-wise multiplication:

$$O_{\text{attn}} = \text{Re-WKV}(K_s, V_s), \quad (6)$$

$$\mathbf{F}_{\text{sm}} = (\sigma(R_s) \odot O_{\text{attn}}) W_{\text{sm}}, \quad (7)$$

where  $\mathbf{F}_{\text{sm}}$  represents the spatial mix output,  $\odot$  denotes element-wise multiplication, and  $W_{\text{sm}}$  is the output projection matrix. The channel mix (cm) module focuses on channel-wise feature fusion. Similar to the spatial mix module, it starts with LN and Omni-Shift, and the receptance  $R_c \in \mathbb{R}^{T \times C}$ , key  $K_c \in \mathbb{R}^{T \times C}$ , and value  $V_c \in \mathbb{R}^{T \times C}$  are computed as follows:

$$\mathbf{F}_c = \text{Omni-Shift}(\text{LN}(\alpha_1 \mathbf{F}_{\text{in}} + \mathbf{F}_{\text{sm}})), \quad (8)$$

$$R_c = \mathbf{F}_c W_{R_c}, \quad K_c = \mathbf{F}_c W_{K_c}, \quad V_c = \gamma(K_c) W_{V_c}, \quad (9)$$

where  $W_{R_c}$ ,  $W_{K_c}$ , and  $W_{V_c}$  are linear projection matrices, and  $\gamma(\cdot)$  is the squared ReLU activation function, which enhances nonlinearity. Notably, the transformation from  $\mathbf{F}_c$  to  $K_c$  to  $V_c$  involves a multi-layer perceptron (MLP) consisting of  $W_{K_c}$ ,  $\gamma(\cdot)$ , and  $W_{V_c}$ , facilitating channel-wise feature fusion. The final channel mix output  $\mathbf{F}_{\text{cm}}$  is obtained through:

$$\mathbf{F}_{\text{cm}} = (\sigma(R_c) \odot V_c) W_{\text{cm}}, \quad (10)$$

where  $W_{\text{cm}}$  is the output projection matrix. Finally, RGEG can be formulated as

$$R = \alpha_2(\alpha_1 \mathbf{F}_{\text{in}} + \mathbf{F}_{\text{sm}}) + \mathbf{F}_{\text{cm}}, \quad (11)$$

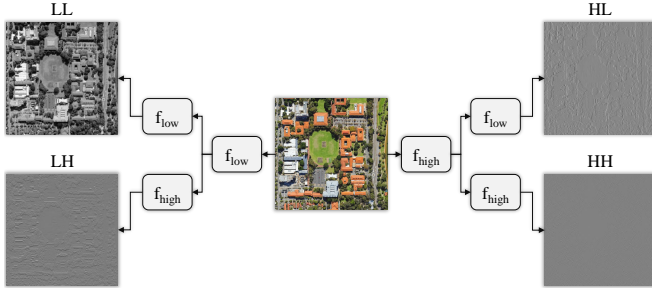


Fig. 5. The SWT uses low-pass and high-pass filters to split the image into frequency components, preserving the original resolution without downsampling.

$$\text{RGE}G^k = WR^l(\dots R^1(\text{RGE}G^{k-1})\dots) + \text{RGE}G^{k-1}, \quad (12)$$

where  $\text{RGE}G^k$  and  $\text{RGE}G^{k-1}$  denote the feature map of the  $k$ -th RGE and  $(k-1)$ -th RGE, respectively.  $R^1$  is the 1-th R-RWKVB.  $W$  is a convolutional layer that serves to enhance the translational equivariance of the RWKV layer, while  $\alpha_1$  and  $\alpha_2$  are learnable scale factors.

#### D. Global–Detail Reconstruction Module

Remote sensing images often exhibit intricate spatial details and large-scale contextual information, necessitating a specialized module to harmonize these features for enhanced reconstruction performance. To effectively integrate the complementary features extracted by the RDEG and the RGE, the GDRM is designed as a fusion mechanism tailored for RSI-SR tasks.

To harmonize and align these two feature representations, the GDRM employs a Permuted Spatial Attention Module (PSAM), which is designed to be computationally efficient and structurally simple. As illustrated in Fig. 3, the module begins by applying a permute operation to the input feature map, reorganizing it into three distinct formats, each capturing specific spatial relationships: Height-Width (HW), Channel-Width (CW), and Height-Channel (HC). Spatial Attention [38] is subsequently applied to each permuted representation independently, enabling the modeling of dependencies along these dimensions. The processed features are then permuted back to their original format, summed together, and scaled by a coefficient. Formally, the aligned feature maps are computed as:

$$\begin{aligned} \mathbf{F}_{\text{CW}}, \mathbf{F}_{\text{HC}} &= \text{Permute}(\text{SA}(\text{Permute}(\mathbf{F}_{\text{in}}))), \\ \mathbf{F}_{\text{HW}} &= \text{SA}(\mathbf{F}_{\text{in}}), \end{aligned} \quad (13)$$

$$\mathbf{F}_{\text{aligned}} = W(\mathbf{F}_{\text{CW}} + \mathbf{F}_{\text{HC}} + \mathbf{F}_{\text{HW}}), \quad (14)$$

where  $\text{SA}(\cdot)$  denotes the spatial attention operation and  $W$  is a fixed coefficient. As illustrated in Fig. 4, the GDRM receives two input feature maps: one capturing local details  $\mathbf{F}_{\text{D}} \in \mathbb{R}^{H \times W \times C}$  from the RDEG branch and another representing global contextual information  $\mathbf{F}_{\text{G}} \in \mathbb{R}^{H \times W \times C}$  from the RGE branch. The GDRM then processes these feature maps through a series of operations, which can be expressed as:

$$\mathbf{F}_{\text{G}} = \text{PSAM}(\mathbf{F}_{\text{G}}), \mathbf{F}_{\text{D}} = \text{PSAM}(\mathbf{F}_{\text{D}}), \quad (15)$$

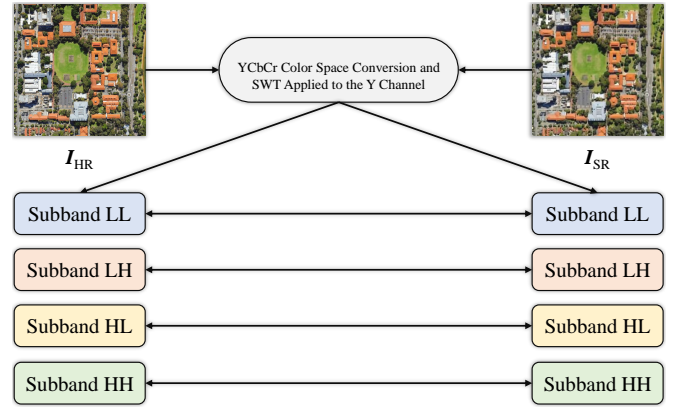


Fig. 6. Wavelet Loss is defined as the sum of  $\mathcal{L}_1$  losses computed for each subband in the wavelet transform.

$$\begin{aligned} \mathbf{F}_{\text{shared}} &= W_{\text{shared}}(\text{cat}(\mathbf{F}_{\text{G}}, \mathbf{F}_{\text{D}})), \\ w &= \sigma W_0(\text{LReLU}(\mathbf{F}_{\text{shared}})), \\ b &= W_1(\mathbf{F}_{\text{shared}}), \end{aligned} \quad (16)$$

$$\mathbf{F}_{\text{GDRM}} = w(\mathbf{F}_{\text{G}} + \mathbf{F}_{\text{D}}) + b. \quad (17)$$

#### E. Wavelet Loss

Due to the unique characteristics of remote sensing imagery, preserving fine-grained details across multiple scales is critical for enhancing spatial resolution while preserving fine-grained spatial details and structural consistency. To address this challenge, we introduce an integrable wavelet-based loss function designed for versatile and effective application across diverse SR models, leveraging the Haar wavelet transform to capture high-frequency details essential for visually and quantitatively improved RSI-SR results.

As illustrated in Fig. 5, the SWT generates one low-frequency (LF) subband, LL, representing the coarse structure of the image, and three high-frequency (HF) subbands, LH, HL, and HH, which encode horizontal, vertical, and diagonal details, respectively. As illustrated in Fig. 6, the wavelet loss function is formulated as the  $\mathcal{L}_1$  distance between the corresponding Haar wavelet subbands of the generated SR image and the HR image. The total wavelet loss is expressed as:

$$\mathcal{L}_{\text{Wavelet}} = \mathbb{E}\left[\sum_j \lambda_j \|\text{Haar}(\mathbf{I}_{\text{HR}})_j - \text{Haar}(\mathbf{I}_{\text{SR}})_j\|_1\right], \quad (18)$$

where  $\mathbf{I}_{\text{HR}}$  and  $\mathbf{I}_{\text{SR}}$  are the HR and SR images,  $\text{Haar}(\cdot)$  denotes the Haar wavelet transform,  $j$  indexes the subbands, and  $\lambda_j$  are scaling factors that balance the importance of each subband. The total wavelet loss is averaged over a minibatch size represented by  $\mathbb{E}[\cdot]$ . By emphasizing high-frequency subbands, the loss effectively enhances edge and texture preservation, while the low-frequency subband ensures structural consistency. The overall loss for the training with wavelet loss is given by

$$\mathcal{L}_{\text{rec}} = \|\mathbf{I}_{\text{HR}} - \mathbf{I}_{\text{SR}}\|_1, \quad (19)$$

$$\mathcal{L} = \mathcal{L}_{\text{rec}} + \mathcal{L}_{\text{Wavelet}}. \quad (20)$$

TABLE I  
Geographical Distribution of Counties in the RSSRD-QH Dataset.

County	Longitude (°E)	Latitude (°N)
Maqin	100.219 to 100.285	34.264 to 34.7
Gande	100.047 to 100.719	34.054 to 34.204
Dari	98.7845 to 98.996	33.485 to 33.925
Maduo	97.929 to 98.129	34.668 to 34.698
Henan	101.374 to 101.759	34.307 to 34.707
Gangcha	100.406 to 100.509	37.351 to 37.671
Tianjun	98.409 to 98.624	37.45 to 37.4855

## IV. EXPERIMENT

### A. Datasets and Evaluation

This paper reports the performance of SR on two remote sensing image datasets, including the publicly available AID dataset [39] and the custom RSSRD-QH dataset.

The AID dataset consists of 30 categories. For each category, the data was randomly split into two equal parts, one for training and the other for testing. Additionally, 20% of the training data was further separated and used as a validation set. Specifically, the training set contained 4,000 images, the validation set 1,000 images, and the test set 5,000 images.

The RSSRD-QH dataset is located in representative watershed units within the Sanjiangyuan region and the Qinghai Lake surrounding area. The geographical distribution of the counties covered by the dataset, including their longitude and latitude ranges, is summarized in Table I. The dataset was collected using unmanned aerial vehicles, with flight altitudes carefully controlled between 30 and 50 meters. The average spatial resolution of the captured imagery is 0.01 meters, providing comprehensive coverage of various landscape elements across different elevation gradients, including terraces, floodplains, gentle slopes, and steep slopes within these watershed units. From each Watershed, we randomly selected 50% of the images for the training set and 50% for the test set, with 20% of the training set randomly selected for validation. This resulted in a training set of 2,242 images, a validation set of 561 images, and a test set of 2,804 images. The HR images in both datasets were  $600 \times 600$  pixels, and the corresponding LR images were  $200 \times 200$  pixels.

The proposed method, along with other competing methods, was evaluated on the test datasets using two classic full-reference metrics: Peak Signal-to-Noise Ratio (PSNR) and Structural Similarity Index (SSIM) [40]. Additionally, the LPIPS [41] metric was used to capture the perceptual quality of the images. Notably, PSNR and SSIM were calculated based on the luminance channel (Y) of the YCbCr color space, while LPIPS evaluated the perceptual similarity between images by extracting features from a pre-trained deep network, specifically the AlexNet model [42], which was employed in this study.

### B. Degradation Model and Implementation Details

We employed both bicubic downsampling and a comprehensive degradation model (CDM) to simulate LR images during training. Based on existing blind SR methods [43], [44] and the characteristics of remote sensing sensors [45], the CDM for

TABLE II  
Ablation studies for the number of RCB. The configuration with 12 RCBs denotes the proposed GDSR model. Bold indicates the model proposed in this work.

RCBs	PSNR/SSIM $\uparrow$	LPIPS $\downarrow$	#Param.	FLOPs	FPS
1	28.96/0.7658	0.3514	5.86M	340.25G	7.3
4	28.96/0.7657	0.3518	7.85M	455.31G	7.0
8	29.00/0.7677	0.3499	10.51M	608.73G	6.7
<b>12</b>	<b>29.03/0.7686</b>	<b>0.3476</b>	<b>13.17M</b>	<b>762.14G</b>	<b>6.4</b>
16	29.01/0.7680	0.3480	15.83M	915.55G	6.1
20	29.03/0.7688	0.3477	18.48M	1068.97G	5.8

LR image synthesis included isotropic Gaussian blur, motion blur, scaling with different interpolation methods, additive Gaussian noise, and JPEG compression noise, all applied in random order.

Our GDSR performed deep feature exploration through 4 RGEGs, RDEGs, and GDRMs. Each RGEG consisted of 6 R-RWKVBs and each RDEG contains 12 RCBs. Empirically, we set the internal channel dimension to  $c = 96$ . For the GDSR\_TC and GDSR\_MC, the RGEG branches correspond to the RTSB and ResidualGroup of SwinIR [14] and MambaIR [18], respectively, with all other settings remaining consistent with GDSR.

During training, each HR image was randomly cropped to a size of  $192 \times 192$  pixels, with the corresponding LR image size being  $64 \times 64$  pixels. The batch size was set to 16, and the Adam optimizer was used with  $\beta_1 = 0.9$  and  $\beta_2 = 0.999$ . The initial learning rate was set to  $1 \times 10^{-4}$ , which was halved at the 100th epoch, with a total of 200 training epochs. All SR models were implemented in the PyTorch framework. The FLOPs results were calculated using an input tensor of size  $1 \times 3 \times 240 \times 240$ , and the computations were performed using torch-operation-counter [46]. The inference times were tested on 300 random images with a size of  $3 \times 240 \times 240$ . All experiments were conducted on an NVIDIA A800 80GB GPU.

### C. Ablation Study

In this section, we discuss the proposed GDSR in depth by investigating the effect of its major components and their variants.

1) *Effect of Key Modules: (a) Effect of RDEG.* To investigate the effect of RDEG on the model performance, we conducted ablation experiments by varying the number of RCBs in RDEG.

The experimental results, presented in Tables II and III, indicated that the model achieved a PSNR of 28.94 dB and an SSIM of 0.7652 when only the RGEG branch was utilized without incorporating RDEG. Adding a single RCB significantly improved the model's performance, increasing the PSNR to 28.96 dB and the SSIM to 0.7658. This improvement highlighted the RCB's capability to capture critical information, thereby enhancing reconstruction quality.

As the number of RCBs increased, further improvements in PSNR and SSIM were observed. For instance, increasing the RCB count from 1 to 20 raised the PSNR from 28.96 dB to 29.03 dB and the SSIM from 0.7658 to 0.7688. However, the rate of improvement diminished as the RCB count increased,

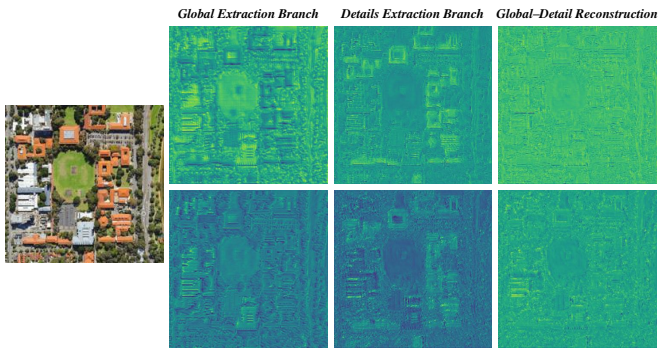


Fig. 7. Feature Visualization Comparisons. The first row presents the feature maps of the 0-th channel, while the second row presents the feature maps of the 1-st channel from the final RREG, RDEG, and GDRM.

TABLE III

Ablation studies for the GDRM. F2B (Feedback to Both RDEG and RREG) refers to the strategy where the output of the GDRM is sent back to both the RDEG and the RREG, enabling updates to the RREG features. F2D (Feedback to RDEG Only) refers to the strategy where the output of the GDRM is sent back only to the RDEG, while the RREG features continue to propagate unchanged from previous layers. Bold indicates the model proposed in this work.

Method	PSNR (dB) $\uparrow$	SSIM $\uparrow$	LPIPS $\downarrow$
RDEG Branch	28.94	0.7656	0.3554
RREG Branch	28.94	0.7652	0.3519
w/o PSAM	29.01	0.7677	0.3485
F2B	29.01	0.7681	0.3476
<b>F2D(GDSR)</b>	<b>29.03</b>	<b>0.7686</b>	<b>0.3476</b>

and beyond a certain threshold, performance even began to decline. This trend suggested that while adding more RCBs initially benefited the model’s output, the marginal gains decreased and eventually plateaued. Additionally, increasing the number of RCBs led to a linear rise in computational complexity, as evidenced by the increase in parameters, FLOPs, and a decrease in FPS. This highlighted the trade-off between performance gains and computational efficiency. Therefore, determining the optimal number of RCBs is crucial in practical applications, especially in scenarios where computational efficiency is a critical factor.

(b) **Effect of GDRM.** To evaluate the effectiveness of the GDRM, we conducted ablation experiments separately using the RDEG and RREG branches. The experimental results were presented in Table III. The comparisons demonstrated that introducing the GDRM significantly improved performance compared to single-branch models. The GDSR model achieved superior PSNR, SSIM, and LPIPS values, indicating that GDSR effectively integrated the local detail information from RDEG and the global contextual information from RREG. Additionally, the incorporation of PSAM enabled GDRM to fuse the information from both branches more effectively.

(c) **Visualization of GDRM.** Fig. 7 visualized the features of the RDEG, RREG branches, and GDRM. We observed that the feature maps from RDEG and RREG were complementary, while GDRM combined features from both branches. This demonstrated that, within the dual-branch structure of GDSR, each branch focused on different features, and fusing these features enabled effective image reconstruction.

Fig. 8 provided visual comparisons under different branches and reconstruction strategies. It was evident that the RREG

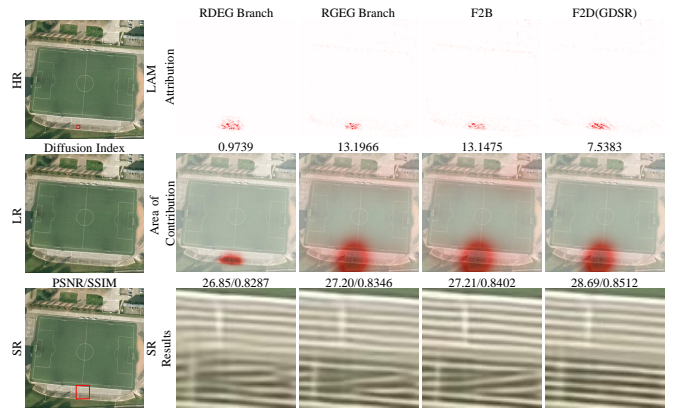


Fig. 8. The visualization of Local Attribution Maps (LAM) [47]. The LAM maps represent the importance of each pixel in the input LR image w.r.t. the SR of the patch marked with a red box. The Diffusion Index (DI) [47] reflects the range of involved pixels. A higher DI represents a wider range of attention.

TABLE IV

Ablation studies for network depth on performance. A depth of 4 denotes the GDSR model, while a depth of 8 denotes the GDSR\_L model. Bold indicates the model proposed in this work.

Depth	PSNR/SSIM $\uparrow$	LPIPS $\downarrow$	#Param.	FLOPs	FPS
1	28.89/0.7633	0.3565	3.65M	211.64G	24.6
2	28.97/0.7663	0.3514	6.82M	395.14G	12.6
<b>4</b>	<b>29.03/0.7686</b>	<b>0.3476</b>	<b>13.17M</b>	<b>762.14G</b>	<b>6.4</b>
6	29.03/0.7686	0.3463	19.52M	1129.14G	4.3
<b>8</b>	<b>29.04/0.7692</b>	<b>0.3456</b>	<b>25.86M</b>	<b>1496.14G</b>	<b>3.2</b>
10	29.05/0.7695	0.3450	32.21M	1863.13G	2.5

branch had a significantly larger receptive field than the RDEG branch and activated more widely distributed pixels for image reconstruction. As a result, the RREG branch achieved better PSNR and SSIM values. Two Global-Detail reconstruction strategies, F2B and F2D, yielded different results. F2B, which sent the reconstructed features back to both RREG and RDEG branches, largely retained the wide receptive field benefits of the RREG branch and similar DI values. However, its SR results were comparable to those of the single RREG branch. In contrast, F2D, which sent the reconstructed features only back to the RDEG branch, achieved DI values between those of the RREG and RDEG branches. The SR results of the F2D strategy showed that it correctly reconstructed textures and delivered more desirable outcomes. This finding aligned with previous studies, which suggested that while expanding the model’s receptive field allowed consideration of a broader range of pixels, it could also lead to incorrect texture reconstruction. This indicated that simply leveraging information from more pixels was insufficient for accurate reconstruction; effectively utilizing pixel information within the receptive field was crucial. As shown in the LAM Attribution map in Fig. 8, the F2D strategy, compared to F2B and the RREG branch, demonstrated a greater contribution of pixels within the corresponding regions to the SR results. In contrast, the distant pixels captured by the wide receptive field of the RREG branch (e.g., pixels in the upper part of the figure) contributed less to the SR results. This suggested that F2D, by routing features exclusively back to the RDEG branch, enabled the model to utilize information more efficiently and reconstruct

TABLE V

Quantitative comparison on AID [39] and RSSRD-QH test set in terms of PSNR, SSIM, and LPIPS, where the 1st, 2nd, and 3rd best performance are highlighted in **red**, **green**, and **blue**, respectively. GDSR\_TC and GDSR\_MC denote the GDSR models with the RGEg branch implemented using Transformer [14] and Mamba [18], respectively. GDSR\_L denotes the GDSR model with a network depth of 8 layers.

Methods	Venue	AID [39]			AID_CDM [39]			RSSRD-QH			RSSRD-QH_CDM		
		PSNR $\uparrow$	SSIM $\uparrow$	LPIPS $\downarrow$	PSNR $\uparrow$	SSIM $\uparrow$	LPIPS $\downarrow$	PSNR $\uparrow$	SSIM $\uparrow$	LPIPS $\downarrow$	PSNR $\uparrow$	SSIM $\uparrow$	LPIPS $\downarrow$
Bicubic	-	27.89	0.7238	0.4400	23.15	0.5238	0.6911	26.45	0.6447	0.4243	22.34	0.3525	<b>0.6993</b>
SRCNN [6]	CVPR'2014	28.22	0.7363	0.3973	23.38	0.5455	0.6569	26.54	0.6512	0.4241	22.44	0.3588	0.7523
SRGAN [8]	CVPR'2017	28.80	0.7597	0.3601	23.78	0.5648	0.6314	26.68	0.6586	0.4170	22.64	0.3759	0.7421
EDSR [9]	CVPR'2017	28.94	0.7653	0.3513	23.91	0.5698	0.6139	26.70	0.6598	0.4141	22.74	0.3817	0.7283
SwinIR [14]	CVPR'2021	28.95	0.7658	0.3512	23.89	0.5705	0.6169	26.70	0.6597	0.4133	22.72	0.3780	0.7432
HAT [15]	CVPR'2023	28.99	0.7671	0.3479	23.99	0.5737	0.6080	26.71	0.6602	0.4111	22.79	0.3823	0.7312
MambaIR [18]	ECCV'2024	<b>29.02</b>	<b>0.7684</b>	0.3487	<b>24.07</b>	<b>0.5763</b>	<b>0.6000</b>	<b>26.72</b>	<b>0.6607</b>	0.4124	22.84	<b>0.3835</b>	0.7387
ConvFormerSR [16]	TGRS'2024	28.90	0.7637	0.3516	23.97	0.5710	0.6118	26.69	0.6603	<b>0.4090</b>	22.77	0.3779	0.7365
FreMamba [20]	TMM'2024	28.96	0.7672	<b>0.3410</b>	23.89	0.5692	0.6148	26.70	0.6601	0.4112	22.60	0.3660	<b>0.7242</b>
<b>GDSR_TC (Ours)</b>	-	28.96	0.7660	0.3500	24.01	0.5717	0.6126	26.71	0.6604	0.4144	22.79	0.3776	0.7401
<b>GDSR_MC (Ours)</b>	-	28.97	0.7668	<b>0.3472</b>	24.03	0.5734	0.6080	26.71	0.6602	0.4107	<b>22.84</b>	0.3819	0.7327
<b>GDSR (Ours)</b>	-	<b>29.03</b>	<b>0.7686</b>	0.3476	<b>24.10</b>	<b>0.5770</b>	<b>0.5986</b>	<b>26.72</b>	<b>0.6612</b>	<b>0.4106</b>	<b>22.86</b>	<b>0.3861</b>	0.7268
<b>GDSR_L (Ours)</b>	-	<b>29.04</b>	<b>0.7692</b>	<b>0.3456</b>	<b>24.15</b>	<b>0.5795</b>	<b>0.5936</b>	<b>26.73</b>	<b>0.6615</b>	<b>0.4098</b>	<b>22.89</b>	<b>0.3875</b>	<b>0.7253</b>

TABLE VI

Quantitative comparison on AID [39] and RSSRD-QH test sets in terms of PSNR, SSIM, and LPIPS. Results trained using Wavelet Loss are compared, where superior or equal performances are highlighted in **red**, and inferior performances are marked in **blue**.

Methods	Venue	AID [39]			AID_CDM [39]			RSSRD-QH			RSSRD-QH_CDM		
		PSNR $\uparrow$	SSIM $\uparrow$	LPIPS $\downarrow$	PSNR $\uparrow$	SSIM $\uparrow$	LPIPS $\downarrow$	PSNR $\uparrow$	SSIM $\uparrow$	LPIPS $\downarrow$	PSNR $\uparrow$	SSIM $\uparrow$	LPIPS $\downarrow$
SRCNN [6]	CVPR'2014	<b>28.25</b>	<b>0.7369</b>	<b>0.3998</b>	<b>23.38</b>	<b>0.5456</b>	<b>0.6609</b>	<b>26.55</b>	<b>0.6498</b>	<b>0.4221</b>	<b>22.44</b>	<b>0.3590</b>	<b>0.7485</b>
SRGAN [8]	CVPR'2017	<b>28.82</b>	<b>0.7605</b>	<b>0.3672</b>	<b>23.80</b>	<b>0.5652</b>	<b>0.6458</b>	<b>26.69</b>	<b>0.6581</b>	<b>0.4183</b>	<b>22.65</b>	<b>0.3760</b>	<b>0.7456</b>
EDSR [9]	CVPR'2017	<b>28.96</b>	<b>0.7658</b>	<b>0.3524</b>	<b>23.94</b>	<b>0.5711</b>	<b>0.6233</b>	<b>26.70</b>	<b>0.6596</b>	<b>0.4128</b>	<b>22.76</b>	<b>0.3821</b>	<b>0.7357</b>
SwinIR [14]	CVPR'2021	<b>28.98</b>	<b>0.7668</b>	<b>0.3533</b>	<b>23.90</b>	<b>0.5704</b>	<b>0.6301</b>	<b>26.71</b>	<b>0.6592</b>	<b>0.4147</b>	<b>22.73</b>	<b>0.3781</b>	<b>0.7488</b>
HAT [15]	CVPR'2023	<b>29.04</b>	<b>0.7692</b>	<b>0.3483</b>	<b>24.01</b>	<b>0.5736</b>	<b>0.6183</b>	<b>26.72</b>	<b>0.6597</b>	<b>0.4137</b>	<b>22.81</b>	<b>0.3829</b>	<b>0.7348</b>
MambaIR [18]	ECCV'2024	<b>29.04</b>	<b>0.7690</b>	<b>0.3521</b>	<b>24.08</b>	<b>0.5767</b>	<b>0.6114</b>	<b>26.72</b>	<b>0.6598</b>	<b>0.4134</b>	<b>22.85</b>	<b>0.3842</b>	<b>0.7388</b>
ConvFormerSR [16]	TGRS'2024	<b>28.93</b>	<b>0.7647</b>	<b>0.3524</b>	<b>23.99</b>	<b>0.5707</b>	<b>0.6281</b>	<b>26.71</b>	<b>0.6591</b>	<b>0.4141</b>	<b>22.77</b>	<b>0.3770</b>	<b>0.7427</b>
FreMamba [20]	TMM'2024	<b>28.94</b>	<b>0.7673</b>	<b>0.3397</b>	<b>23.89</b>	<b>0.5682</b>	<b>0.6318</b>	<b>26.70</b>	<b>0.6599</b>	<b>0.4130</b>	<b>22.64</b>	<b>0.3698</b>	<b>0.7130</b>
<b>GDSR_TC (Ours)</b>	-	<b>28.99</b>	<b>0.7670</b>	<b>0.3522</b>	<b>24.02</b>	<b>0.5719</b>	<b>0.6237</b>	<b>26.72</b>	<b>0.6595</b>	<b>0.4162</b>	<b>22.79</b>	<b>0.3776</b>	<b>0.7437</b>
<b>GDSR_MC (Ours)</b>	-	<b>29.00</b>	<b>0.7675</b>	<b>0.3512</b>	<b>24.06</b>	<b>0.5742</b>	<b>0.6159</b>	<b>26.72</b>	<b>0.6591</b>	<b>0.4122</b>	<b>22.84</b>	<b>0.3815</b>	<b>0.7395</b>
<b>GDSR (Ours)</b>	-	<b>29.04</b>	<b>0.7689</b>	<b>0.3522</b>	<b>24.12</b>	<b>0.5774</b>	<b>0.6121</b>	<b>26.73</b>	<b>0.6603</b>	<b>0.4116</b>	<b>22.88</b>	<b>0.3862</b>	<b>0.7313</b>
<b>GDSR_L (Ours)</b>	-	<b>29.06</b>	<b>0.7694</b>	<b>0.3499</b>	<b>24.16</b>	<b>0.5791</b>	<b>0.6069</b>	<b>26.73</b>	<b>0.6603</b>	<b>0.4119</b>	<b>22.90</b>	<b>0.3875</b>	<b>0.7314</b>

accurate textures by correctly leveraging the pixels within the receptive field.

**(d) Effect of Network Depth on Performance.** To investigate the effect of network depth on the performance of GDSR, we varied the shared depth of both the RDEG and RGEg branches while keeping other design parameters constant. As illustrated in Table IV, the experimental outcomes consistently demonstrated an enhancement in performance with deeper networks. Moreover, an evaluation of the trade-offs in terms of computational complexity was conducted. As the network depth increased, the model’s parameter count, FLOPS, and FPS were also scaled accordingly. These results supported the effectiveness of GDSR’s dual-branch design, where the shared depth allowed for both high-quality super-resolution and manageable computational overhead.

2) *Effect of Wavelet Loss:* To evaluate the effectiveness of incorporating Wavelet Loss in training, ablation experiments were conducted comparing models trained with Wavelet Loss to those using only  $\mathcal{L}_1$  Loss. These experiments spanned multiple datasets and degradation models, employing a variety of architectures. The results consistently demonstrated that

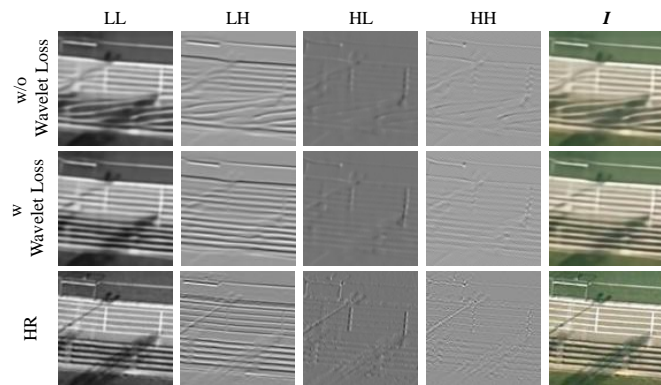


Fig. 9. Visualization of Wavelet Loss effectiveness in MambaIR, showing LL, LH, HL, HH, and SR results for the playground track reconstruction.

Wavelet Loss improves PSNR, with SSIM also showing notable enhancement in most cases. On the RSSRD-QH dataset, a decrease in SSIM performance was observed, which was attributed to the complexity of basin images, characterized by intricate textures and diverse structures. Wavelet Loss emphasized high-frequency details, which didn’t align with SSIM’s



TABLE VII

Quantitative comparison with SOTA SR methods across 30 scene categories on AID [39], where the best and second best PSNR/SSIM performance are highlighted in **red** and **blue**, respectively.

Categories	Bicubic		SRGAN [8]		EDSR [9]		HAT [15]		MambaIR [18]		ConvFormerSR [16]		FreMamba [20]		GDSR (Ours)	
	PSNR $\uparrow$	SSIM $\uparrow$	PSNR $\uparrow$	SSIM $\uparrow$	PSNR $\uparrow$	SSIM $\uparrow$	PSNR $\uparrow$	SSIM $\uparrow$	PSNR $\uparrow$	SSIM $\uparrow$	PSNR $\uparrow$	SSIM $\uparrow$	PSNR $\uparrow$	SSIM $\uparrow$	PSNR $\uparrow$	SSIM $\uparrow$
Airport	27.43	0.7387	28.48	0.7765	28.63	0.7823	28.69	0.7837	<b>28.72</b>	<b>0.7856</b>	28.59	0.7805	28.68	0.7851	<b>28.72</b>	<b>0.7853</b>
Bare Land	34.45	0.8344	34.84	0.8422	34.92	0.8439	34.94	0.8445	<b>34.96</b>	<b>0.8449</b>	34.91	0.8436	34.93	0.8444	<b>34.97</b>	<b>0.8449</b>
Baseball Field	29.19	0.7786	30.27	0.8094	30.42	0.8137	30.45	0.8144	<b>30.52</b>	<b>0.8160</b>	30.35	0.8123	30.43	0.8147	<b>30.53</b>	<b>0.8160</b>
Beach	31.32	0.7947	31.86	0.8082	31.94	0.8103	31.99	<b>0.8117</b>	<b>32.00</b>	<b>0.8118</b>	31.94	0.8096	31.95	0.8113	<b>32.00</b>	0.8115
Bridge	30.19	0.8063	31.27	0.8312	31.46	0.8353	31.52	0.8363	<b>31.56</b>	<b>0.8372</b>	31.42	0.8339	31.52	0.8368	<b>31.57</b>	<b>0.8371</b>
Center	25.76	0.6980	27.18	0.7590	27.38	0.7665	27.47	0.7694	<b>27.51</b>	<b>0.7706</b>	27.33	0.7645	27.43	0.7692	<b>27.51</b>	<b>0.7705</b>
Church	23.09	0.6084	24.41	0.6807	24.56	0.6895	24.61	0.6920	<b>24.65</b>	<b>0.6941</b>	24.52	0.6875	24.56	0.6919	<b>24.67</b>	<b>0.6947</b>
Commercial	26.72	0.7178	27.59	0.7582	27.73	0.7645	27.77	0.7660	<b>27.81</b>	<b>0.7679</b>	27.68	0.7623	27.72	0.7659	<b>27.81</b>	<b>0.7681</b>
D-Residential	23.45	0.6301	24.46	0.6922	24.60	0.7004	24.64	0.7026	<b>24.69</b>	<b>0.7051</b>	24.56	0.6985	24.60	0.7029	<b>24.70</b>	<b>0.7056</b>
Desert	37.14	0.8869	37.54	0.8933	37.58	0.8944	<b>37.63</b>	<b>0.8951</b>	37.62	0.8949	37.58	0.8941	37.60	0.8946	<b>37.62</b>	<b>0.8950</b>
Farmland	32.32	0.7934	33.18	0.8166	33.33	0.8212	33.35	0.8216	<b>33.42</b>	<b>0.8236</b>	33.30	0.8202	33.39	0.8235	<b>33.43</b>	<b>0.8240</b>
Forest	27.67	0.6411	27.84	0.6514	27.90	0.6558	<b>27.95</b>	<b>0.6605</b>	27.95	0.6604	27.88	0.6552	27.92	0.6598	<b>27.97</b>	<b>0.6616</b>
Industrial	26.29	0.7063	27.43	0.7566	27.62	0.7647	27.67	0.7669	<b>27.71</b>	<b>0.7689</b>	27.56	0.7621	27.62	0.7665	<b>27.72</b>	<b>0.7690</b>
Meadow	32.07	0.7100	32.33	0.7136	32.38	0.7157	32.40	0.7167	<b>32.41</b>	<b>0.7172</b>	32.37	0.7154	32.39	<b>0.7175</b>	<b>32.42</b>	<b>0.7172</b>
M-Residential	26.32	0.6578	27.40	0.7055	27.55	0.7124	27.58	0.7136	<b>27.63</b>	<b>0.7159</b>	27.52	0.7113	27.55	0.7140	<b>27.64</b>	<b>0.7164</b>
Mountain	28.05	0.6978	28.41	0.7127	28.48	0.7163	<b>28.50</b>	<b>0.7184</b>	28.50	0.7183	28.46	0.7152	28.45	0.7171	<b>28.50</b>	<b>0.7183</b>
Park	27.14	0.7060	27.77	0.7332	27.87	0.7383	27.91	0.7406	<b>27.93</b>	<b>0.7415</b>	27.83	0.7365	27.86	0.7395	<b>27.94</b>	<b>0.7422</b>
Parking	24.11	0.7310	26.18	0.8059	26.51	0.8159	26.68	0.8205	<b>26.76</b>	0.8225	26.46	0.8145	26.70	<b>0.8226</b>	<b>26.77</b>	<b>0.8228</b>
Playground	29.33	0.7723	30.70	0.8132	30.94	0.8200	31.03	0.8216	<b>31.10</b>	<b>0.8235</b>	30.88	0.8182	31.03	0.8230	<b>31.12</b>	<b>0.8237</b>
Pond	28.76	0.7559	29.38	0.7749	29.46	0.7781	29.49	0.7790	<b>29.51</b>	<b>0.7796</b>	29.44	0.7769	29.46	0.7788	<b>29.51</b>	<b>0.7796</b>
Port	25.83	0.7727	26.94	0.8207	27.11	0.8255	27.18	0.8273	<b>27.21</b>	<b>0.8283</b>	27.05	0.8237	27.13	0.8267	<b>27.21</b>	<b>0.8278</b>
Railway Station	27.00	0.6965	27.87	0.7347	28.04	0.7434	28.11	0.7456	<b>28.13</b>	<b>0.7474</b>	27.99	0.7404	28.07	0.7461	<b>28.14</b>	<b>0.7477</b>
Resort	26.78	0.7160	27.67	0.7547	27.81	0.7601	27.86	0.7622	<b>27.89</b>	<b>0.7634</b>	27.78	0.7588	27.82	0.7619	<b>27.91</b>	<b>0.7638</b>
River	29.29	0.7201	29.74	0.7378	29.81	0.7412	29.84	0.7426	<b>29.85</b>	<b>0.7430</b>	29.79	0.7401	29.80	0.7422	<b>29.86</b>	<b>0.7431</b>
School	25.81	0.7046	26.81	0.7503	26.96	0.7568	27.00	0.7587	<b>27.04</b>	<b>0.7604</b>	26.91	0.7546	26.94	0.7577	<b>27.05</b>	<b>0.7607</b>
S-Residential	25.71	0.5790	26.15	0.6001	26.22	0.6055	26.25	0.6070	<b>26.27</b>	<b>0.6079</b>	26.21	0.6046	26.23	0.6075	<b>26.27</b>	<b>0.6077</b>
Square	27.51	0.7286	28.71	0.7782	28.90	0.7847	28.96	0.7870	<b>28.99</b>	<b>0.7881</b>	28.85	0.7831	28.92	0.7868	<b>29.01</b>	<b>0.7882</b>
Stadium	26.23	0.7241	27.55	0.7771	27.75	0.7845	27.82	0.7873	<b>27.85</b>	<b>0.7882</b>	27.68	0.7823	27.78	0.7867	<b>27.85</b>	<b>0.7881</b>
Storage Tanks	25.15	0.6667	26.25	0.7190	26.39	0.7255	26.41	0.7264	<b>26.45</b>	<b>0.7287</b>	26.33	0.7233	26.39	0.7274	<b>26.45</b>	<b>0.7286</b>
Viaduct	26.77	0.6817	27.70	0.7225	27.88	0.7310	27.91	0.7325	<b>27.98</b>	<b>0.7361</b>	27.81	0.7277	27.87	0.7326	<b>27.98</b>	<b>0.7363</b>
Average	27.89	0.7238	28.80	0.7597	28.94	0.7653	28.99	0.7671	<b>29.02</b>	<b>0.7684</b>	28.90	0.7637	28.96	0.7672	<b>29.03</b>	<b>0.7686</b>

focus on global structural similarity. A decline in LPIPS was also observed across all experiments with Wavelet Loss, due to its emphasis on high-frequency details and structural accuracy. The prioritization of fine-grained features introduced perceptual differences, as captured by LPIPS. Nonetheless, the substantial improvements in PSNR and SSIM underscored the overall effectiveness of Wavelet Loss in producing high-quality SR images, guiding the correct reconstruction of textures across various architectures.

As shown in Figure 9, despite MambaIR’s global receptive field and its superior performance in experiments, the model still struggled to accurately reconstruct certain textures without Wavelet Loss. The inclusion of Wavelet Loss significantly improved the reconstruction, particularly in the high-frequency components (LH, HL, HH), where fine-grained details were preserved. This highlights Wavelet Loss’s role in guiding the model to recover intricate structures and accurately reconstruct complex textures, thereby enhancing overall image quality.

#### D. Comparisons With State-of-the-Art

1) *Comparative Methods*: CNN-based models, including SRCNN [6] and EDSR [9]; GAN-based models, including SRGAN [8]; Transformer-based models, including SwinIR [14] and HAT [15]; CNN-Transformer hybrid models, including ConvFormerSR [16]; and Mamba-based models, including MambaIR [18] and FreMamba [20], were involved in evaluating the SR performance of our GDSR against SOTA methods on RSI-SR. We also report the results of our model variants,

GDSR\_TC and GDSR\_MC, as well as the large-scale variant GDSR\_L.

2) *Quantitative Evaluations*: The quantitative results on the AID and RSSRD-QH datasets are presented in Table V. Our proposed GDSR and GDSR\_L models achieved superior performance across all metrics, demonstrating their remarkable SR capabilities in diverse remote sensing tests. On the AID and RSSRD-QH datasets, GDSR achieved performance comparable to MambaIR. On the AID\_CDM and RSSRD-QH\_CDM datasets, GDSR’s advantages became more pronounced. It achieved PSNR, SSIM, and LPIPS values of 24.10, 0.5770, and 0.5986, respectively, on AID\_CDM, and PSNR and SSIM values of 22.86 and 0.3861, respectively, on RSSRD-QH\_CDM, significantly outperforming other methods. GDSR\_L consistently led across all tests, and both GDSR\_TC and GDSR\_MC achieved performance comparable to FreMamba on the AID and RSSRD-QH datasets while demonstrating substantial improvements on the AID\_CDM and RSSRD-QH\_CDM datasets. Specifically, GDSR\_MC achieved a 0.14 dB PSNR improvement on AID\_CDM and a 0.24 dB improvement on RSSRD-QH\_CDM compared to FreMamba.

To further evaluate the generalization capability of the super-resolution models across diverse remote sensing scenarios, we report the PSNR and SSIM results across 30 scene categories in the AID dataset, as shown in Table VII. As evidenced, GDSR exhibited stronger generalization capability compared to state-of-the-art methods, achieving the best performance in nearly all remote sensing scenarios. Specifically,

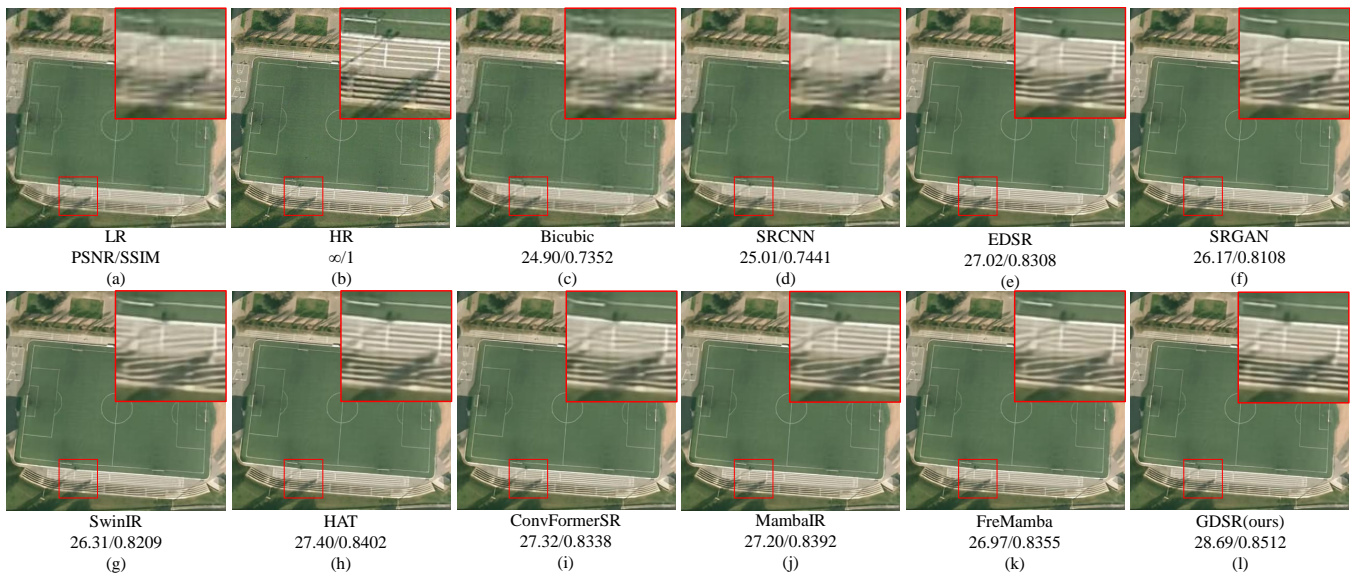


Fig. 10. Visual comparisons of our GDSR with CNN-, GAN-, Transformer-, and Mamba-based methods on the AID dataset’s "playground\_161" image with scale  $\times 3$ . Zoom in for better observation.

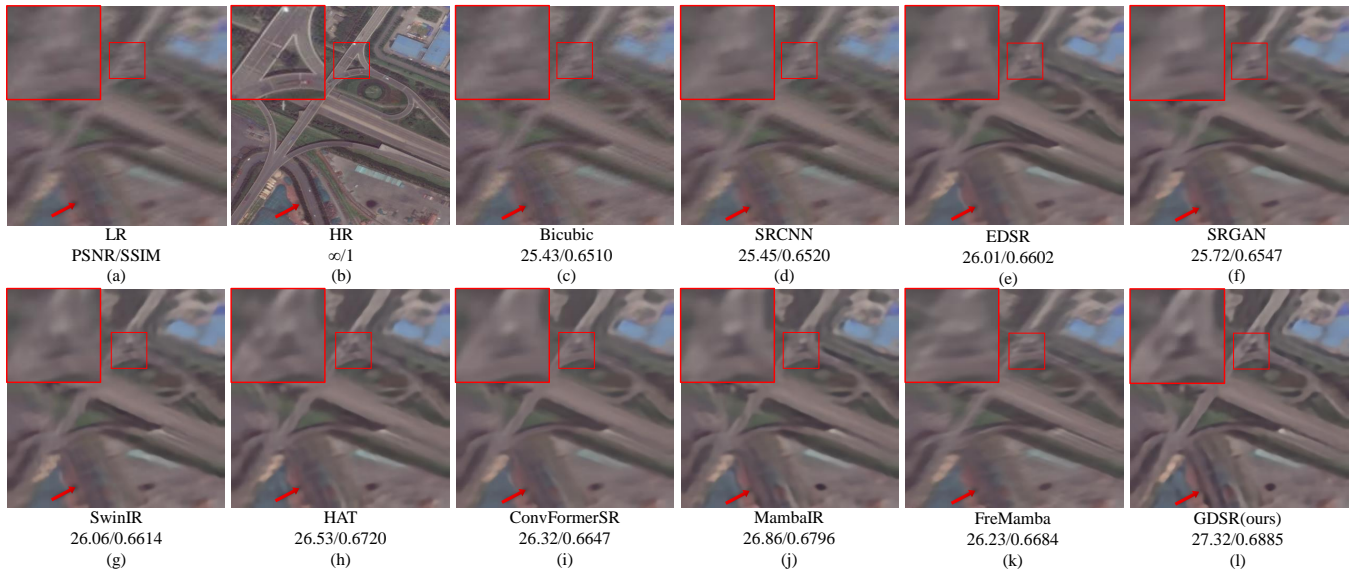


Fig. 11. Visual comparisons of our GDSR with CNN-, GAN-, Transformer-, and Mamba-based methods on the AID\_CDM dataset’s "viaduct\_398" image with scale  $\times 3$ . Zoom in for better observation.

for the "Parking" and "Playground" scenes, GDSR outperformed HAT by 0.09 dB in PSNR and by 0.0023 and 0.0021 in SSIM, respectively. Additionally, in the most complex categories, such as "Church" and "DenseResidential," GDSR also achieved the best performance.

Moreover, as the receptive field of the models increased, performance trended upward for CNN-based EDSR, Transformer-based SwinIR, and Mamba-based MambaIR. This aligned with our experimental results on the RLEG Branch and RDEG Branch, where larger receptive fields enabled the activation of more pixels for image reconstruction, enhancing performance. However, the results from MambaIR and FreMamba, along with the experiments on F2B and F2C, indicated that spatial global modeling in complex remote sensing images had reached a bottleneck. Simply increasing

the receptive field no longer yielded significant performance gains. A more practical solution was to effectively utilize large receptive fields to activate the appropriate regions and pixels for accurate image reconstruction. The outstanding generalization capability and superior performance of GDSR aligned with our motivation to address the challenges of large-scale remote sensing images efficiently through the introduction of a global-detail dual-branch structure.

3) *Complexity and Efficiency Evaluation:* To evaluate the complexity and computational efficiency of our proposed models, we conducted quantitative assessments across various metrics. As shown in Table VIII, the bicubic interpolation technique inherently avoids the need for parameter optimization, resulting in the fastest inference speed within our evaluation scope. The CNN-based model achieved the highest inference

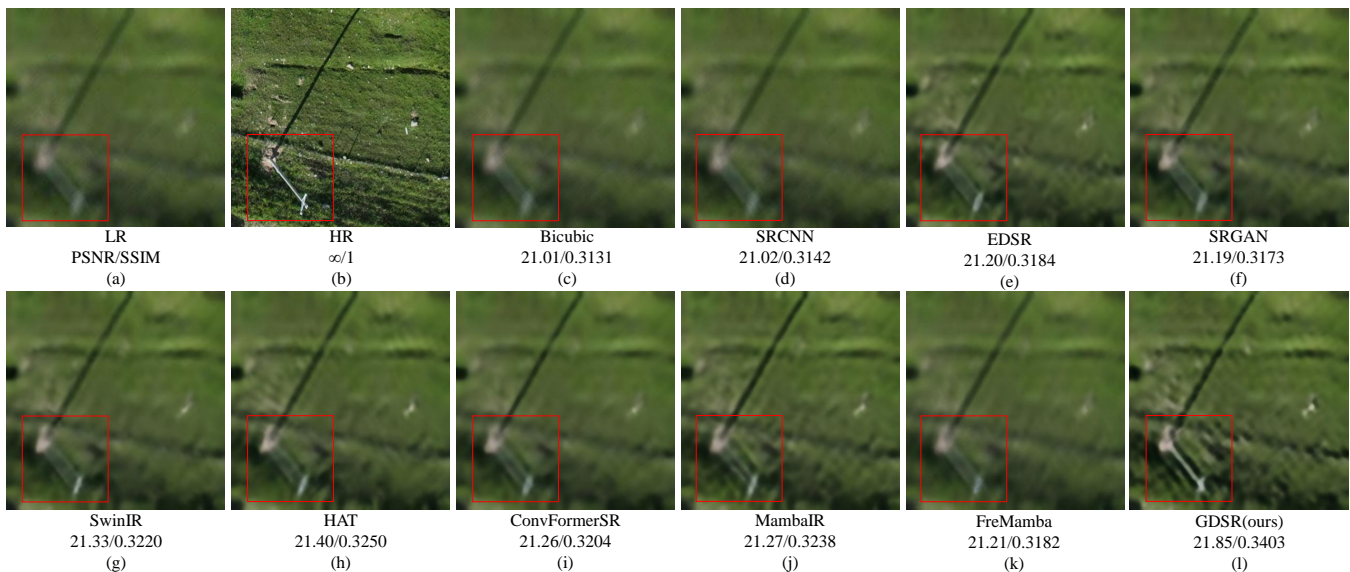


Fig. 12. Visual comparisons of our GDSR with CNN-, GAN-, Transformer-, and Mamba-based methods on the RSSRD-QH\_CDM dataset with scale  $\times 3$ .

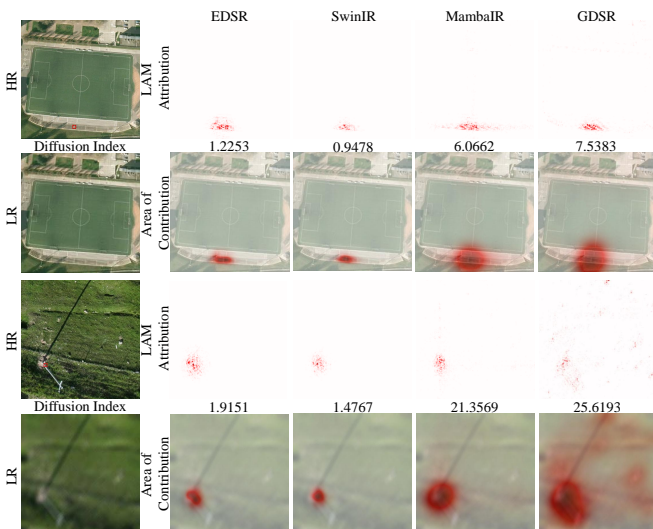


Fig. 13. The visualization of LAM on datasets AID and RSSRD-QH\_CDM.

speed among all tested deep learning models, primarily due to the inherent efficiency of convolutional parallel operations. The EDSR model, with its deep residual structure, had the largest number of parameters and FLOPs, yet achieved inference speeds several times faster than other architectures.

Transformer-based models, such as SwinIR and HAT, exhibited slower inference speeds compared to CNN-based models but achieved significant performance gains. Models based on Mamba, including MambaIR and FreMamba, leveraged their linear complexity and optimized inference processes, delivering superior performance along with relatively faster inference speeds. ConvFormerSR, which integrated Swin Transformer with CNN architectures, achieved faster inference speeds while maintaining competitive performance.

GDSR, by incorporating RWKV with CNN, not only reduced the parameter count but also achieved inference speeds several times faster than Transformer- and Mamba-based

TABLE VIII  
Comparisons of model complexity and efficiency.

Model	#Param.	FLOPs	FPS
Bicubic	-	-	21505.6
SRCNN [6]	0.02M	10.47G	533.1
SRGAN [8]	1.55M	107.68G	151.9
EDSR [9]	43.68M	2519.95G	15.5
SwinIR [14]	16.62M	1005.01G	2.3
HAT [15]	20.81M	1467.38G	2.2
MambaIR [18]	15.11M	838.91G	2.8
ConvFormerSR [16]	16.49M	994.90G	3.2
FreMamba [20]	11.46M	516.21G	2.5
<b>GDSR_TC (Ours)</b>	12.83M	758.82G	3.3
<b>GDSR_MC (Ours)</b>	13.99M	788.28G	4.1
<b>GDSR (Ours)</b>	13.17M	762.14G	6.4
<b>GDSR_L (Ours)</b>	25.86M	1496.14G	3.2

models, while delivering enhanced performance. GDSR\_TC and GDSR\_MC further optimized performance by combining Swin Transformer and Mamba with CNN, leading to a reduction in parameter size and improved inference speed, without sacrificing performance. GDSR\_L, which increased the network depth, consistently outperformed other models in experimental evaluations while maintaining reasonable inference speeds. As demonstrated in Tables II, III, and IV, these results underscore the superiority of the Global-Detail dual-branch architecture design.

Comparing Tables VIII and V reveals that the complexity of our proposed model is comparable to most state-of-the-art models, while its efficiency is superior, and its performance is significantly better. These results highlight the practical potential of our model, demonstrating an effective balance between computational efficiency and performance, making it well-suited for real-world applications.

4) *Qualitative Results*: Visual comparisons on AID, AID\_CDM, and RSSRD-QH\_CDM with a scale factor of  $\times 3$  are presented in Fig. 10, Fig. 11, and Fig. 12. From these visual results, it was evident that our proposed GDSR was capable of restoring sharp edges and showcasing richer

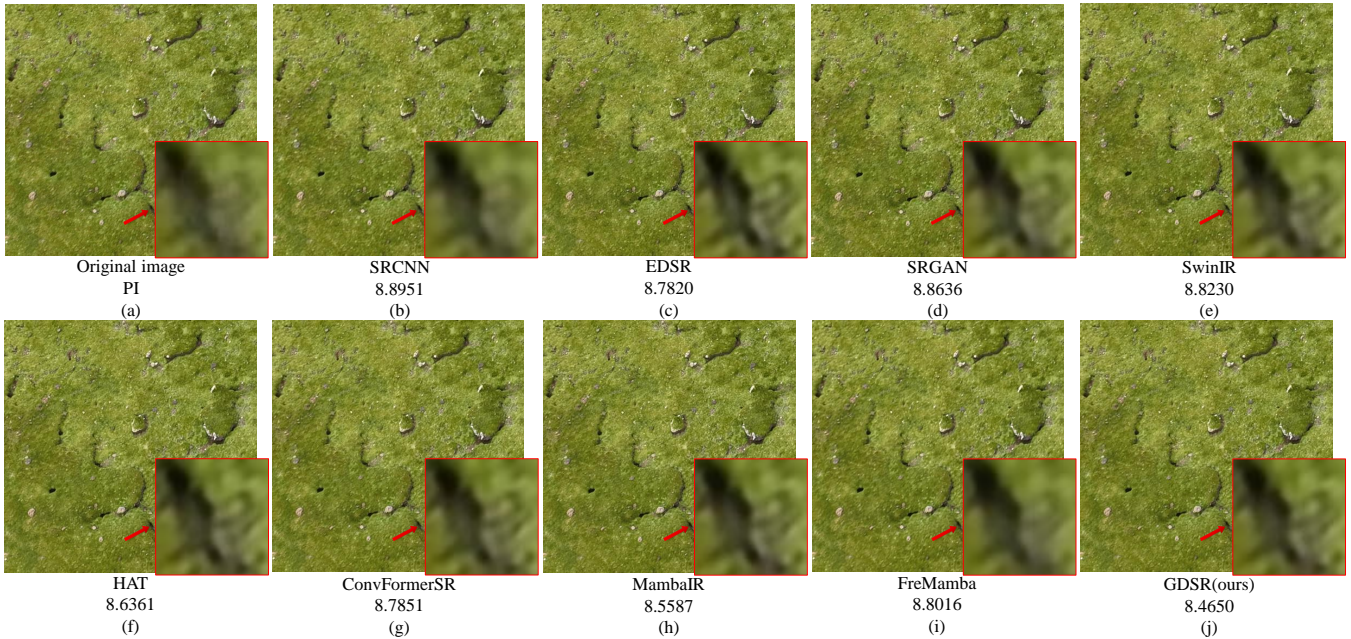


Fig. 14. Visualizations of Real-World Images for better observation of mouse holes. Zoom in for better observation. We tested the model trained with RSSRD-QH\_CDM on real drone images. A lower value indicates better reconstruction quality when using the Perception Index (PI) metric [48].

textures, particularly in capturing critical high-frequency details in remote sensing images. For instance, when comparing the reconstructed "playground\_161" in Fig. 10, the closest competing Transformer-based method HAT, the hybrid CNN-Transformer method ConvFormerSR, and the Mamba-based model MambaIR all failed to reconstruct the high-resolution lines on the runway. Only the proposed GDSR accurately restored these details. Furthermore, as illustrated in Fig. 11 for "viaduct\_398," under more complex degradation scenarios, GDSR effectively reconstructed the contours, whereas other SR models failed to accurately represent the detailed structure. In Fig. 12, a comparison of the visual results for the RSSRD-QH\_CDM dataset showed that the original image, after CDM degradation, appeared heavily blurred and lost its distinctive columnar features. Only the proposed GDSR was able to accurately recover the outline of the original image.

The LAM comparisons in Fig. 13, based on Figs. 10 and 12, demonstrated that GDSR benefitted from the superior long-range modeling capability of RGEg, enabling it to leverage more pixels during the SR process. Additionally, the strong detail extraction capability of RDEg allowed GDSR to utilize pixels correctly for reconstruction. Specifically, for the RSSRD-QH\_CDM dataset, when large-scale and global information was present, CNN- and Transformer-based SR networks struggled to extract sufficient information, and while the Mamba-based SR network activated a large number of pixels, they failed to use them correctly for reconstruction. In contrast, thanks to the effective integration of RGEg and RDEg, the GDSR-generated results significantly outperformed other SR models. Moreover, GDSR surpassed MambaIR in terms of a diffusion index by 25.6193, indicating that by incorporating an RWKV with a larger receptive field into RGEg, GDSR could better capture global information in images with more such features, leading to a higher diffusion index. These visual

comparisons further validated the effectiveness of GDSR in capturing and reconstructing details in remote sensing images, highlighting the powerful pixel utilization capability brought by our global-detail dual-branch structure.

5) *Real-World Image Testing on the Sanjiangyuan Region:* To further evaluate the model's performance in real-world scenarios, we tested it on remote sensing images from real-world environments. As shown in Fig. 14, the image depicts an alpine meadow grassland type, with surface features such as cracks, scattered rocks, and numerous small "mouse holes." These mouse holes are depressions or openings on the ground, and the distribution of rodents is significant for studying the primary grassland type, the alpine meadow, in Qinghai Province. Their presence can impact the biodiversity, productivity, and ecological function of the alpine meadows. However, due to the limitations in drone flight conditions and resolution, the raw images suffer from motion blur and loss of details. These issues hinder accurate observation of key features such as surface textures and the depth of the mouse holes. By applying SR techniques, our GDSR effectively enhanced the clarity of these fine details, sharpened the edges around the mouse holes, and restored the surface texture. This improvement is crucial for accurate environmental analysis, as the restored landscape provides more precise data for studying biodiversity conservation and the enhancement of ecological functions in the alpine meadow ecosystem of Qinghai Province.

## V. CONCLUSION

In this study, we first introduce the Receptance Weighted Key Value for remote sensing image super-resolution. GDSR effectively models the global dependencies of large-scale remote sensing images while incorporating local details, all with linear complexity and significantly improved inference

speed. Specifically, we design an efficient and effective Global-Detail dual-branch architecture that correctly activates more pixels spatially for image reconstruction. To combine global and local representations, we propose GDRM, which adaptively adjusts the features of the dual branches and fuses them. Additionally, we introduce Wavelet Loss to help the model better capture high-frequency details in remote sensing image super-resolution tasks. Extensive quantitative and qualitative experiments on the AID, AID\_CDM, RSSRD-QH, and RSSRD-QH\_CDM benchmarks demonstrate that our GDSR outperforms state-of-the-art CNN-, Transformer-, and Mamba-based SR models in remote sensing image super-resolution tasks. The proposed Wavelet Loss also enhances the performance of various models in remote sensing image super-resolution tasks.

This study focuses solely on  $\times 3$  SR, limiting the flexibility to explore SR at different scales. Experiments show that excessive high-frequency components introduced by Wavelet Loss can lead to a decline in perceptual quality. In future work, we plan to extend our GDSR to include more scaling factors, further demonstrating its robustness and effectiveness. Additionally, we aim to optimize Wavelet Loss to improve its perceptual enhancement.

## REFERENCES

- [1] T. Sung, Y. Kang, and J. Im, "Enhancing satellite-based wildfire monitoring: Advanced contextual model using environmental and structural information," *IEEE Transactions on Geoscience and Remote Sensing*, vol. 62, pp. 1–16, 2024.
- [2] F. Li, T. Yigitcanlar, M. Nepal, K. Nguyen, and F. Dur, "Machine learning and remote sensing integration for leveraging urban sustainability: A review and framework," *Sustainable Cities and Society*, vol. 96, p. 104653, 2023.
- [3] H. Ijaz, R. Ahmad, R. Ahmed, W. Ahmed, Y. Kai, and W. Jun, "A uav-assisted edge framework for real-time disaster management," *IEEE Transactions on Geoscience and Remote Sensing*, vol. 61, pp. 1–13, 2023.
- [4] K. Li, S. Yang, R. Dong, X. Wang, and J. Huang, "Survey of single image super-resolution reconstruction," *IET Image Processing*, vol. 14, no. 11, pp. 2273–2290, 2020.
- [5] J. Huang, K. Li, and X. Wang, "Single image super-resolution reconstruction of enhanced loss function with multi-gpu training," in *2019 IEEE Intl Conf on Parallel & Distributed Processing with Applications, Big Data & Cloud Computing, Sustainable Computing & Communications, Social Computing & Networking (ISPA/BDCloud/SocialCom/SustainCom)*. IEEE, 2019, pp. 559–565.
- [6] C. Dong, C. C. Loy, K. He, and X. Tang, "Image super-resolution using deep convolutional networks," *IEEE transactions on pattern analysis and machine intelligence*, vol. 38, no. 2, pp. 295–307, 2015.
- [7] J. Kim, J. K. Lee, and K. M. Lee, "Accurate image super-resolution using very deep convolutional networks," in *Proceedings of the IEEE conference on computer vision and pattern recognition*, 2016, pp. 1646–1654.
- [8] C. Ledig, L. Theis, F. Huszár, J. Caballero, A. Cunningham, A. Acosta, A. Aitken, A. Tejani, J. Totz, Z. Wang *et al.*, "Photo-realistic single image super-resolution using a generative adversarial network," in *Proceedings of the IEEE conference on computer vision and pattern recognition*, 2017, pp. 4681–4690.
- [9] B. Lim, S. Son, H. Kim, S. Nah, and K. Mu Lee, "Enhanced deep residual networks for single image super-resolution," in *Proceedings of the IEEE conference on computer vision and pattern recognition workshops*, 2017, pp. 136–144.
- [10] S. Lei, Z. Shi, and W. Mo, "Transformer-based multistage enhancement for remote sensing image super-resolution," *IEEE Transactions on Geoscience and Remote Sensing*, vol. 60, pp. 1–11, 2022.
- [11] D. He and Y. Zhong, "Deep hierarchical pyramid network with high-frequency-aware differential architecture for super-resolution mapping," *IEEE Transactions on Geoscience and Remote Sensing*, vol. 61, pp. 1–15, 2023.
- [12] W. Luo, Y. Li, R. Urtasun, and R. Zemel, "Understanding the effective receptive field in deep convolutional neural networks," *Advances in neural information processing systems*, vol. 29, 2016.
- [13] Z. Yang, H. Zhang, D. Zhao, B. Wei, and Y. Xu, "Restore-rwkv: Efficient and effective medical image restoration with rwkv," *arXiv preprint arXiv:2407.11087*, 2024.
- [14] J. Liang, J. Cao, G. Sun, K. Zhang, L. Van Gool, and R. Timofte, "Swinir: Image restoration using swin transformer," in *Proceedings of the IEEE/CVF international conference on computer vision*, 2021, pp. 1833–1844.
- [15] X. Chen, X. Wang, J. Zhou, Y. Qiao, and C. Dong, "Activating more pixels in image super-resolution transformer," in *Proceedings of the IEEE/CVF Conference on Computer Vision and Pattern Recognition (CVPR)*, June 2023, pp. 22 367–22 377.
- [16] J. Li, Y. Meng, C. Tao, Z. Zhang, X. Yang, Z. Wang, X. Wang, L. Li, and W. Zhang, "Convformers: Fusing transformers and convolutional neural networks for cross-sensor remote sensing imagery super-resolution," *IEEE Transactions on Geoscience and Remote Sensing*, vol. 62, pp. 1–15, 2024.
- [17] L. Gao, H. Liu, M. Yang, L. Chen, Y. Wan, Z. Xiao, and Y. Qian, "Stranfuse: Fusing swin transformer and convolutional neural network for remote sensing image semantic segmentation," *IEEE journal of selected topics in applied earth observations and remote sensing*, vol. 14, pp. 10 990–11 003, 2021.
- [18] H. Guo, J. Li, T. Dai, Z. Ouyang, X. Ren, and S.-T. Xia, "Mambair: A simple baseline for image restoration with state-space model," in *European Conference on Computer Vision*. Springer, 2025, pp. 222–241.
- [19] A. Gu and T. Dao, "Mamba: Linear-time sequence modeling with selective state spaces," *arXiv preprint arXiv:2312.00752*, 2023.
- [20] Y. Xiao, Q. Yuan, K. Jiang, Y. Chen, Q. Zhang, and C.-W. Lin, "Frequency-assisted mamba for remote sensing image super-resolution," *IEEE Transactions on Multimedia*, vol. 26, pp. 1–14, 2024.
- [21] B. Peng, E. Alcaide, Q. Anthony, A. Albalak, S. Arcadinho, S. Biderman, H. Cao, X. Cheng, M. Chung, M. Grella *et al.*, "Rwkv: Reinventing rns for the transformer era," *arXiv preprint arXiv:2305.13048*, 2023.
- [22] B. Peng, D. Goldstein, Q. Anthony, A. Albalak, E. Alcaide, S. Biderman, E. Cheah, X. Du, T. Ferdinan, H. Hou *et al.*, "Eagle and finch: Rwkv with matrix-valued states and dynamic recurrence," *arXiv preprint arXiv:2404.05892*, 2024.
- [23] H. Yuan, X. Li, L. Qi, T. Zhang, M.-H. Yang, S. Yan, and C. C. Loy, "Mamba or rwkv: Exploring high-quality and high-efficiency segment anything model," *arXiv preprint arXiv:2406.19369*, 2024.
- [24] N. Park and S. Kim, "How do vision transformers work?" in *International Conference on Learning Representations*, 2022.
- [25] Y. Zhang, Y. Tian, Y. Kong, B. Zhong, and Y. Fu, "Residual dense network for image super-resolution," in *Proceedings of the IEEE conference on computer vision and pattern recognition*, 2018, pp. 2472–2481.
- [26] Y. Zhang, K. Li, K. Li, L. Wang, B. Zhong, and Y. Fu, "Image super-resolution using very deep residual channel attention networks," in *Proceedings of the European conference on computer vision (ECCV)*, 2018, pp. 286–301.
- [27] B. Niu, W. Wen, W. Ren, X. Zhang, L. Yang, S. Wang, K. Zhang, X. Cao, and H. Shen, "Single image super-resolution via a holistic attention network," in *Computer Vision—ECCV 2020: 16th European Conference, Glasgow, UK, August 23–28, 2020, Proceedings, Part XII 16*. Springer, 2020, pp. 191–207.
- [28] Y. Long, X. Wang, M. Xu, S. Zhang, S. Jiang, and S. Jia, "Dual self-attention swin transformer for hyperspectral image super-resolution," *IEEE Transactions on Geoscience and Remote Sensing*, vol. 61, pp. 1–12, 2023.
- [29] Z. Chen, Y. Zhang, J. Gu, L. Kong, and X. Yang, "Recursive generalization transformer for image super-resolution," in *ICLR*, 2024.
- [30] Y. Duan, W. Wang, Z. Chen, X. Zhu, L. Lu, T. Lu, Y. Qiao, H. Li, J. Dai, and W. Wang, "Vision-rwkv: Efficient and scalable visual perception with rwkv-like architectures," *arXiv preprint arXiv:2403.02308*, 2024.
- [31] Z. Fei, M. Fan, C. Yu, D. Li, and J. Huang, "Diffusion-rwkv: Scaling rwkv-like architectures for diffusion models," *arXiv preprint arXiv:2404.04478*, 2024.
- [32] I. Daubechies, "Ten lectures on wavelets," *Society for industrial and applied mathematics*, 1992.
- [33] H. Huang, R. He, Z. Sun, and T. Tan, "Wavelet-srnet: A wavelet-based cnn for multi-scale face super resolution," in *Proceedings of the IEEE international conference on computer vision*, 2017, pp. 1689–1697.
- [34] X. Deng, R. Yang, M. Xu, and P. L. Dragotti, "Wavelet domain style transfer for an effective perception-distortion tradeoff in single

- image super-resolution,” in *Proceedings of the IEEE/CVF international conference on computer vision*, 2019, pp. 3076–3085.
- [35] J. Xin, J. Li, X. Jiang, N. Wang, H. Huang, and X. Gao, “Wavelet-based dual recursive network for image super-resolution,” *IEEE Transactions on Neural Networks and Learning Systems*, vol. 33, no. 2, pp. 707–720, 2022.
- [36] C. Korkmaz, A. M. Tekalp, and Z. Dogan, “Training generative image super-resolution models by wavelet-domain losses enables better control of artifacts,” in *Proceedings of the IEEE/CVF Conference on Computer Vision and Pattern Recognition*, 2024, pp. 5926–5936.
- [37] S. E. Finder, R. Amoyal, E. Treister, and O. Freifeld, “Wavelet convolutions for large receptive fields,” in *European Conference on Computer Vision*. Springer, 2025, pp. 363–380.
- [38] S. Woo, J. Park, J.-Y. Lee, and I. S. Kweon, “Cbam: Convolutional block attention module,” in *Proceedings of the European conference on computer vision (ECCV)*, 2018, pp. 3–19.
- [39] G.-S. Xia, J. Hu, F. Hu, B. Shi, X. Bai, Y. Zhong, L. Zhang, and X. Lu, “Aid: A benchmark data set for performance evaluation of aerial scene classification,” *IEEE Transactions on Geoscience and Remote Sensing*, vol. 55, no. 7, pp. 3965–3981, 2017.
- [40] Z. Wang, A. Bovik, H. Sheikh, and E. Simoncelli, “Image quality assessment: from error visibility to structural similarity,” *IEEE Transactions on Image Processing*, vol. 13, no. 4, pp. 600–612, 2004.
- [41] R. Zhang, P. Isola, A. A. Efros, E. Shechtman, and O. Wang, “The unreasonable effectiveness of deep features as a perceptual metric,” in *Proceedings of the IEEE conference on computer vision and pattern recognition*, 2018, pp. 586–595.
- [42] A. Krizhevsky, I. Sutskever, and G. E. Hinton, “Imagenet classification with deep convolutional neural networks,” *Advances in neural information processing systems*, vol. 25, 2012.
- [43] J. Gu, H. Lu, W. Zuo, and C. Dong, “Blind super-resolution with iterative kernel correction,” in *Proceedings of the IEEE/CVF conference on computer vision and pattern recognition*, 2019, pp. 1604–1613.
- [44] X. Wang, L. Xie, C. Dong, and Y. Shan, “Real-esrgan: Training real-world blind super-resolution with pure synthetic data,” in *Proceedings of the IEEE/CVF international conference on computer vision*, 2021, pp. 1905–1914.
- [45] R. Dong, L. Mou, L. Zhang, H. Fu, and X. X. Zhu, “Real-world remote sensing image super-resolution via a practical degradation model and a kernel-aware network,” *ISPRS Journal of Photogrammetry and Remote Sensing*, vol. 191, pp. 155–170, 2022.
- [46] S. Moustafa, “Torch operation counter,” <https://github.com/SamirMoustafa/torch-operation-counter>, 2023.
- [47] J. Gu and C. Dong, “Interpreting super-resolution networks with local attribution maps,” in *Proceedings of the IEEE/CVF Conference on Computer Vision and Pattern Recognition*, 2021, pp. 9199–9208.
- [48] Y. Blau, R. Mechrez, R. Timofte, T. Michaeli, and L. Zelnik-Manor, “The 2018 pirm challenge on perceptual image super-resolution,” in *Proceedings of the European conference on computer vision (ECCV) workshops*, 2018, pp. 0–0.